REPORT DOCUMENTATION PAGE

Form Approved
OMB No. 0704-0188

1. AGENCY USE ONLY *(Leave blank)*	2. REPORT DATE	3. REPORT TYPE AND DATES COVERED
	September 1992	Technical Paper

4. TITLE AND SUBTITLE
Stagnation-Point Heat-Transfer Rate Predictions at Aeroassist Flight Conditions

5. FUNDING NUMBERS
WU 506-40-91-02

6. AUTHOR(S)
Roop N. Gupta, Jim J. Jones, and William C. Rochelle

7. PERFORMING ORGANIZATION NAME(S) AND ADDRESS(ES)
NASA Langley Research Center
Hampton, VA 23681-0001

8. PERFORMING ORGANIZATION REPORT NUMBER
L-17039

9. SPONSORING/MONITORING AGENCY NAME(S) AND ADDRESS(ES)
National Aeronautics and Space Administration
Washington, DC 20546-0001

10. SPONSORING/MONITORING AGENCY REPORT NUMBER
NASA TP-3208

11. SUPPLEMENTARY NOTES
Gupta: Langley Research Center, Hampton, Virginia;
Jones: Analytical Mechanics Associates, Hampton, Virginia;
Rochelle: Lockheed Engineeering & Sciences Co., Houston, Texas.

12a. DISTRIBUTION/AVAILABILITY STATEMENT
Unclassified–Unlimited

Subject Category 34

12b. DISTRIBUTION CODE

13. ABSTRACT *(Maximum 200 words)*

Results are presented for the stagnation-point heat-transfer rates used in the design process of the Aeroassist Flight Experiment (AFE) vehicle over its entire aeropass trajectory. The prediction methods used in this investigation demonstrate the application of computational fluid dynamics (CFD) techniques to a wide range of flight conditions and their usefulness in a design process. The heating rates were computed by a viscous-shock-layer (VSL) code at the lower altitudes and by a Navier-Stokes (N-S) code for the higher altitude cases. For both these methods, finite-rate chemically reacting gas was considered, and a temperature-dependent wall-catalysis model was used. The wall temperature for each case was assumed to be radiative equilibrium temperature, based on total (radiative plus convective) heating. The radiative heating was estimated by using a correlation equation. Wall slip was included in the N-S calculation method, and this method implicitly accounts for shock slip. The N-S/VSL combination of prediction methods was established by comparison with the published results of the benchmark flow-field code LAURA at lower altitudes and comparison with the direct simulation Monte Carlo results for the higher altitude cases of this study. For the purpose of obtaining the design heating rates over the entire forward face of the vehicle, a boundary-layer method (BLIMP code) that employs reacting chemistry and surface catalysis was used. The ratio of the VSL or N-S method prediction to that obtained from the boundary-layer method at the stagnation point is used to define an adjustment factor, which accounts for the errors involved in using the boundary-layer method.

14. SUBJECT TERMS
Hypersonic flow; Stagnation-point heat transfer; Low- and High-altitude flight conditions; Navier-Stokes; Viscous shock layer; Boundary-layer methods; Aeroassist Flight Experiment

15. NUMBER OF PAGES
19

16. PRICE CODE
A03

17. SECURITY CLASSIFICATION OF REPORT	18. SECURITY CLASSIFICATION OF THIS PAGE	19. SECURITY CLASSIFICATION OF ABSTRACT	20. LIMITATION OF ABSTRACT
Unclassified	Unclassified		

NSN 7540-01-280-5500

Standard Form 298(Rev. 2-89)
Prescribed by ANSI Std. Z39-18
298-102

NASA-Langley, 1992

Summary

Results are presented for the stagnation-point heat-transfer rates used in the design process of the Aeroassist Flight Experiment (AFE) vehicle over its entire aeropass trajectory. The flight experiment had been proposed to obtain measurements of surface and flow-field quantities for an improved understanding of the aerothermal nature of the flow at hypervelocity, low-density aeropass conditions and to provide a data base to verify existing prediction methods. The prediction methods used in this investigation demonstrate the application of computational fluid dynamics (CFD) techniques to a wide range of flight conditions and their usefulness in a design process. The heating rates were computed by a viscous-shock-layer (VSL) code at the lower altitudes, and by a Navier-Stokes (N-S) code for the higher altitude cases. For both these methods, finite-rate chemically reacting gas was considered, and a temperature-dependent wall-catalysis model was used. The wall temperature for each case was assumed to be radiative equilibrium temperature, based on total (radiative plus convective) heating. The radiative heating was estimated by using a correlation equation. Wall slip was included in the N-S calculation method, and this method implicitly accounts for shock slip. The N-S/VSL combination of prediction methods was established by comparison with the published results of the benchmark flow-field code LAURA at lower altitudes, and comparison with the direct simulation Monte Carlo results for the higher altitude cases of this study.

For the purpose of obtaining the design heating rates over the entire forward face of the vehicle, a boundary-layer method (BLIMP code) that employs reacting chemistry and surface catalysis was used. The ratio of the viscous-shock-layer or Navier-Stokes method prediction to that obtained from the boundary-layer method at the stagnation point is used to define an adjustment factor, which accounts for the discrepancies involved in using the boundary-layer method. This adjustment factor and the boundary-layer prediction were used to obtain the design values of heating rate.

Symbols

AF	adjustment factor, $\frac{q_{\mathrm{VSL}}}{q_{\mathrm{BL}}}$ or $\frac{q_{\mathrm{N-S}}}{q_{\mathrm{BL}}}$
C_*	Chapman-Rubesin constant, $\frac{\mu_* T_\infty}{\mu_\infty T_*}$
C_H	heat-transfer coefficient, $\frac{q_c}{\frac{1}{2}\rho_\infty U_\infty^3}$
c_p	specific heat at constant pressure
K^2	Cheng's rarefaction parameter, $\frac{\mathrm{Re}_\infty}{\gamma_\infty M_\infty^2 C_*}$
M	Mach number
n	distance normal to the surface
Δn	grid spacing in normal direction
q	heat-transfer rate
Re	Reynolds number, $\frac{\rho U R_n}{\mu}$
Re_*	equivalent postshock Reynolds number, $\frac{\rho_\infty U_\infty R_n}{\mu_*}$
R_n	vehicle nose radius
T	temperature
T_o	ideal gas stagnation temperature, $\frac{U_\infty^2}{2c_{p\infty}}$
T_*	reference temperature, taken here as $\frac{T_o + T_w}{2}$
t	time
U	velocity
x, y, z	vehicle Cartesian coordinates, see figure 1
γ	specific heat ratio
ε	rarefaction parameter defined in equation (7)
ζ	$\frac{\gamma - 1}{2\gamma}$
μ	viscosity
μ_*	viscosity evaluated from Sutherland's law at temperature T_*
ρ	density

Subscripts:

c	convective
h	altitude
r	radiative
ref	reference (see eqs. (8)–(10))
s	postshock
t	total
w	wall
∞	ambient free stream
$*$	conditions based on reference temperature T_*

Acronyms:

AFE	Aeroassist Flight Experiment
BL	boundary layer
BLIMP	Boundary-Layer Integral Matrix Procedure
CFD	computational fluid dynamics
DSMC	direct simulation Monte Carlo
LAURA	Langley Aerothermodynamic Upwind Relaxation Algorithm
N-S	Navier-Stokes
TPS	thermal protection system
VSL	viscous shock layer

Introduction

The technology of aeroassist (i.e., the use of an atmospheric pass to modify the orbit of a space vehicle) has frequently been proposed as a promising mode for future space missions, as noted, for example, in reference 1. The principal advantage of aeroassist is the saving of weight by reducing the fuel requirements for orbit modulation; it follows that the heat shield required for the aeroassist maneuver must be designed with a minimum impact on spacecraft weight. Thus it is highly desirable to have engineering tools suitable for accurate prediction of heat transfer at the high-altitude conditions of an aeroassist trajectory. However, as discussed in reference 2, flight at aeroassist conditions is characterized by such factors as a highly viscous, reacting chemistry with thermal nonequilibrium effects, shock and wall slip effects, and nonequilibrium radiation. In this regard, the aeroassist mission design differs from that for an entry mission, where the peak heating occurs at much lower altitudes. Thus, past experience in design and analysis of vehicle heat shields for entry has not provided adequate technology development or engineering tools to support the design of aeroassist vehicle heat shields.

The present work was performed in support of the Aeroassist Flight Experiment (AFE), a project that NASA initiated to gather flight data in the flight regime that would be typical for future aeroassist missions. Even though the justification for the AFE mission was lack of adequate engineering tools, or benchmark data to verify such tools for heat shield design, still it was necessary to surmount these problems in order to design the heat shield for the AFE vehicle itself.

Consequently, a considerable effort has been expended to develop computational flow-field methods needed for the design and performance prediction of the AFE heat shield. While the AFE was still in the design stages, budgetary and priority considerations caused the cancellation of the AFE mission. Nevertheless, the planning activity for this mission generated significant advances in computational flow-field technology for treating nonequilibrium, radiating shock-layer flows. This paper presents a portion of that computational activity: specifically, the advancements made in the prediction of stagnation-point heat-transfer rate, and the capability to employ a combination of these methods to allow estimation of heating rate for any time during the aeropass.

The procedure adopted for AFE design activity was to calculate the stagnation-point heating with a combination of a viscous-shock-layer (VSL) method (ref. 3) at the lower altitudes and a Navier-Stokes (N-S) method (ref. 4) at the higher altitudes. With these stagnation-point results as foundation, approximate heating distributions with the boundary-layer method (ref. 5) were obtained for the forebody design.

This paper presents first the analysis that was made to verify the accuracy of the VSL and N-S codes for the range of conditions of the AFE aeropass and then compares the predicted stagnation-point heat-transfer rate to that predicted by the boundary-layer method. The design methodology takes into account the effects of shock-layer chemical nonequilibrium, finite wall catalysis, wall slip and shock slip, and the contribution of shock-layer radiation to the total heating rate. The verification process is made over a range of free-stream states spanning from entry interface, at the border of continuum flow, by comparison to the direct simulation Monte Carlo method, to the perigee condition, using results from a full three-dimensional Navier-Stokes code. This range covers more than three orders of magnitude in Reynolds number. The ratio of the combined VSL/N-S results to the boundary-layer results, termed the adjustment factor, is shown as a function of pertinent parameters.

Methodology

This section provides a discussion of the forebody configuration of the AFE vehicle, the flow-field model and properties used, and brief descriptions of the computational methods and radiative heating correlation employed.

Configuration

The configuration of the AFE vehicle forebody is an ellipsoidal nose tangent to an elliptical cone. The

base of the cone is raked off at an angle of 17° to the normal to the body axis, and a skirt section is attached to the cone. See figure 1. The geometry, which is defined in reference 6, is completely analytic. Since the present report is concerned primarily with the stagnation-point heat transfer, only the nose region is considered here. The radius of the nose in the plane of symmetry (the smaller radius of the ellipsoid) is 7.54 ft (2.3 m). In the other plane of symmetry of the ellipsoid, the radius is 11.46 ft (3.49 m). It should be noted that none of the present calculation methods considered a full three-dimensional geometry. The computational configuration considered for the present methods was an axially symmetric representation of the AFE, consisting of a spherical segment nose ($R_n = 7.1$ ft $= 2.16$ m) and a 60° half-angle cone. This effective nose radius was selected because the resultant convective heating prediction at the peak heating condition was found to be the same as that calculated by the benchmark LAURA code (ref. 7) for the full three-dimensional configuration at an angle of attack of 0°.

Free-Stream State

The free-stream conditions for the present calculations are taken from the AFE trajectory identified for the design calculations as Baseline 5 trajectory. Cases are selected covering the time period for which the vehicle is within the sensible atmosphere. Table I gives the free-stream conditions considered herein. Some of the pertinent free-stream parameters are shown in figure 2. Figure 2(a) illustrates the velocity-altitude variation, while figure 2(b) shows the velocity and Reynolds number variation with time. Time is measured from the instant when the spacecraft has descended to an altitude of 400 000 ft. The free-stream thermodynamic state properties were taken as a function of altitude from the trajectory calculation, which used the NASA Marshall Space Flight Center Global Reference Atmosphere. The version of the atmosphere used is identified as GRAM86, which is derived from that described in reference 8. The values of various parameters

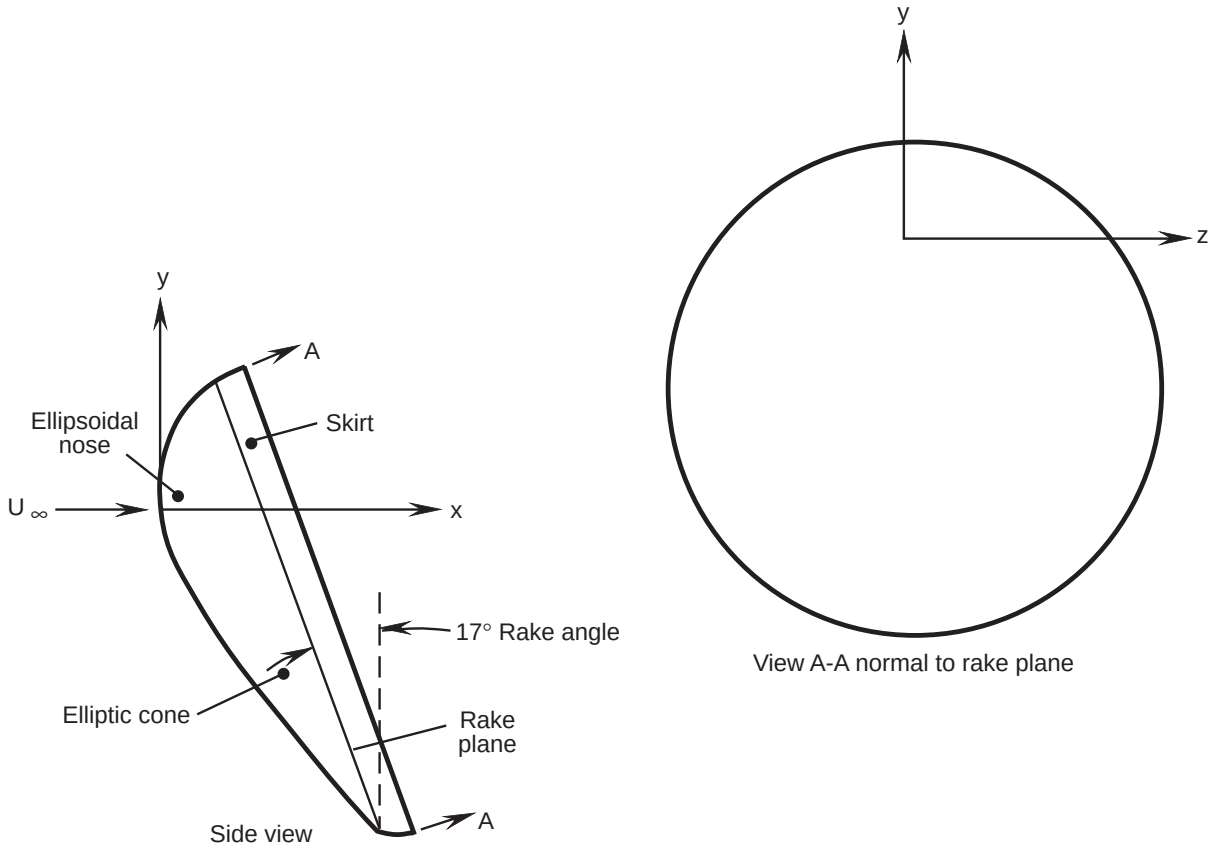

Figure 1. AFE vehicle geometry.

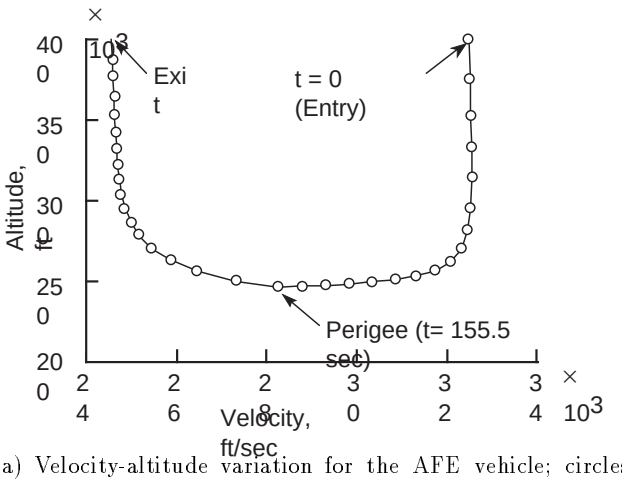

(a) Velocity-altitude variation for the AFE vehicle; circles represent points used for calculation.

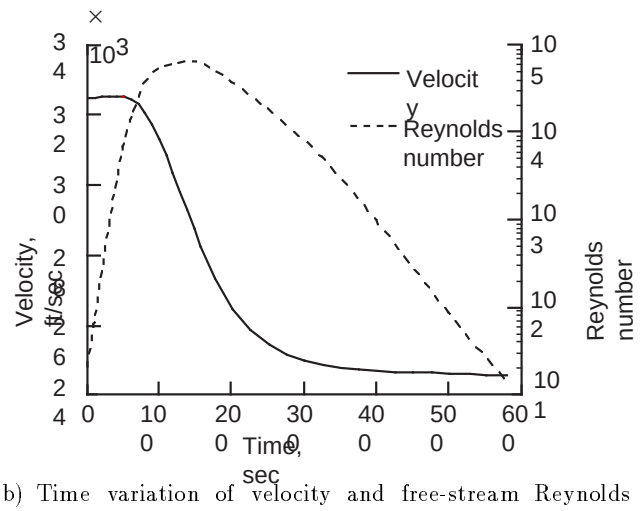

(b) Time variation of velocity and free-stream Reynolds number.

Figure 2. Variation of free-stream parameters for the AFE trajectory.

employed for correlation (altitude, M, Re_∞, Re_*, K^2, and ε) are given in table II. The use of these parameters will be discussed subsequently.

Flow Characteristics

Several characteristics dominate the shock-layer flow field in the range of free-stream conditions for aeroassist vehicles:

1. Most of the shock-layer flow is chemically reacting nonequilibrium flow, with thermal nonequilibrium conditions at the higher altitudes. The calculation methods used in the present work use either 5-species (N, O, NO, N_2, O_2) or 11-species (N, O, NO, N_2, O_2, NO^+, N^+, O^+, N_2^+, O_2^+, e^-) chemical reaction models, but they each consider thermal equilibrium only. The 5-species model was employed with the viscous-shock-layer and boundary-layer methods, whereas the 11-species model was used in the Navier-Stokes calculations. A check was made (at the computed peak-heating condition) to see the effect of the number of species considered, by making 1 VSL calculation with 11 species. The number of species did not have a significant effect on the computed heating rate for the case considered.

2. Highly viscous and merged shock layers prevail. Free-stream Reynolds number based on nose radius varies from less than 20 to nearly 10^5. The viscous-shock-layer method considers viscous effects for the entire shock layer, but assumes a thin shock wave. The stagnation-region Navier-Stokes method computes the thickened shock, implicitly accounting for shock slip. Wall-slip effects (ref. 9) have also been included in this method. The boundary-layer method does not consider any of these effects, which are major sources of difference in the present comparison, especially at higher altitudes.

3. A strong influence of wall catalytic effects on the recombination of dissociated species is observed at lower altitudes. A significant portion of the heat energy brought to the wall comes as a result of the diffusion of atoms, with their accompanying latent heat of dissociation. If the surface is noncatalytic, this heat is not delivered to the wall; if the surface is fully catalytic, all this heat is deposited. As shown in reference 10, the reaction-cured glass coating used to seal the surface of the heat-shield tiles has a rather low energy recombination coefficient, and the specific value of this coefficient is sharply temperature dependent. The importance of this wall temperature effect is illustrated in figure 3, which presents calculations using the VSL method, for which several values are assumed for the wall temperature, but all other conditions remain constant. The data of reference 10 indicate that the wall reaction rate coefficients for both oxygen and nitrogen atoms attain maximum values near 1600 K and decrease sharply for wall temperatures greater or less than this value. As seen in figure 3, the value of the computed heating rate is closely tied to the assumed wall temperature when this model of wall catalysis is used. Consequently, any comparison of heating prediction methods must use similar assumptions regarding wall temperature. All the current solutions have modeled the wall recombination coefficient similar to the data of reference 10, and the solutions have been iterated so that the wall temperature is essentially equal to the radiative equilibrium value for the predicted total heat-transfer rate. For each of the methods, a surface emissivity of 0.85 was assumed, and the solution

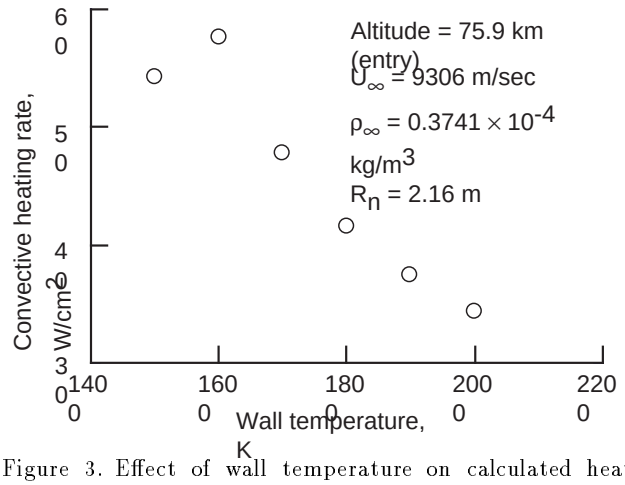

Figure 3. Effect of wall temperature on calculated heat-transfer rate for reaction-cured glass tile coating material.

method was iterated until the wall temperature converged to within 2 K.

4. Radiative transfer in the flow field can be significant. For the free-stream conditions and configuration considered here, the surface heating mode is primarily convective, but the radiative heating is large enough that it may not be neglected in computing the equilibrium wall temperature to assess thermal protection system (TPS) design. Indeed, for a larger vehicle, the radiative transfer might be the dominant mode. None of the present calculation methods couple the radiative flux terms in the solution method, but for the purpose of computing equilibrium wall temperature based on total (radiative plus convective) heat transfer, an estimate of the nonequilibrium radiative heating rate has been made. The radiative heating component in this work was estimated by the equation of reference 11. This equation is provided in a subsequent section.

Computational Methods

Viscous-shock-layer (VSL) method. The viscous-shock-layer code described in reference 3 was used in the present work for the lower altitude calculations. As shown in reference 12, the VSL method, even with surface-slip and shock-slip conditions considered, gives erroneous results at the higher altitudes. At these altitudes the higher order terms (left out of the normal momentum equation in the VSL equations) become significant and result in breakdown of the application of these equations. At lower altitudes, however, the higher order terms are insignificant and the VSL equations give quite accurate results (ref. 3). The VSL code employed here used a 5-species air model, mentioned earlier, and a temperature-dependent wall-catalysis model taken from reference 10. Since these calculations were restricted to low-altitude cases only, no surface-slip or shock-slip boundary conditions were implemented in the code. The VSL computational domain encompassed all the subsonic portion of the shock-layer flow; the solution was continued to a supersonic outflow boundary. For the present VSL (and N-S) calculations, an appropriate grid size was established for the peak heating condition at an altitude of about 76 km through a grid-refinement study of the surface heat-transfer rate. For other altitude calculations, the grid size was varied in relation to the 76-km-altitude grid by employing the relation

$$(\Delta n)_h = (\Delta n)_{h=76\,\mathrm{km}} \frac{[\mu_{\mathrm{ref}}/\,(\rho_\infty U_\infty R_n)]_h}{[\mu_{\mathrm{ref}}/\,(\rho_\infty U_\infty R_n)]_{h=76\,\mathrm{km}}} \qquad (1)$$

Navier-Stokes (N-S) method. The stagnation region Navier-Stokes code described in reference 4 was used in the present work for the lower density cases, where the flow may be too rarefied to justify the simplifying assumptions of the VSL method. An 11-species nonequilibrium chemistry model was employed. The nose radius used was 7.1 ft (2.16 m), in agreement with the VSL method. Solutions were run with and without the wall-slip condition. However, only results with wall slip are used in the AFE design calculation. The wall-catalysis model is consistent with the other methods.

Boundary-layer method (BLIMP code). The boundary-layer calculations reported here employed the 1988 version of the Boundary-Layer Integral Matrix Procedure (BLIMP88) code as described in reference 5. Pressure distributions and metric coefficients were obtained with the BLUNT2D inviscid code of reference 13. This method has been used to provide an engineering approach for computing the heating over the vehicle forebody. With the BLIMP code as the engineering method, a reacting boundary layer with surface catalytic effects can be considered. Along several rays originating from the stagnation point, the BLIMP code was used to compute the heating distribution. For each ray, no cross flow was considered; the configuration could be considered to be the body generated by rotating that ray about the wind vector. For the results presented here, the ray in the plane of symmetry was used, so the effective nose radius was 7.54 ft (2.3 m). These results were computed with chemical nonequilibrium conditions in the boundary layer for a 5-species air model, assuming equilibrium boundary-layer edge conditions. Finite wall catalysis was modeled with the data of reference 10.

Radiative Heating Calculation

An estimate of the nonequilibrium radiative heat-transfer rate has been included in the present work by using a correlation given in reference 9. In this correlation, the stagnation-point radiation heating, q_r, is given as

$$\log(q_r) = 0.3542 + 0.5646\frac{U_\infty}{1000} + \left(0.306 + 0.066\frac{U_\infty}{1000}\right)\log(\rho_\infty R_n) \quad (2)$$

where the units are as follows:

q_r	W/cm^2
U_∞	m/sec
ρ_∞	kg/m^3
R_n	m

It should be noted that equation (2) must be used with caution: it is only an approximation to a very complex calculation, which itself is very much in need of experimental confirmation.

In this study, equation (2) was used to estimate the radiative contribution to the total heating so as to compute a realistic radiative equilibrium wall temperature. For the VSL and N-S methods, a nose radius of 9.0 ft (2.74 m) was used in equation (2) because this produced the same thickness shock layer with the VSL code as was computed by the benchmark LAURA code (ref. 7) for the full three-dimensional (3-D) AFE forebody. It may be noted that the mean of the two principal radii of the ellipsoidal nose is 9.5 ft, so the computed value is close to what one would intuitively expect. However, the BLIMP calculations used a nose radius of 7.5 ft (2.286 m) for the radiative calculation because that value was consistent with the geometric radius used for the convective heating calculation. The difference in assumed nose radii between the VSL method and the BLIMP method resulted in a small difference in computed radiative heating, which thereby influenced the radiative-equilibrium wall temperature. This inconsistency in methods was examined near the peak radiative heating condition, where it might be expected to have maximum impact. For this test, the VSL method was run using a nose radius of 7.1 ft for the convective calculation, but using both 7.5 ft and 9.0 ft for nose radius in the radiative heating estimate. The difference in computed radiative heating caused by the difference in nose radius resulted in a wall temperature difference of about 8 K. The change in convective heating caused by this difference in wall temperature was 1 percent. It was deemed, therefore, that the inconsistency in estimating radiative heating was not sufficient to alter conclusions when comparing results from the different computational methods and would become a part of the adjustment factor correction.

Thermodynamic and Transport Properties

The thermodynamic and transport properties employed in the VSL and N-S codes are those of reference 14, which are valid to a temperature of 30 000 K. Mixture viscosity is obtained by the method of Armaly and Sutton (ref. 15), and the mixture thermal conductivity is computed by the Mason and Saxena relation of reference 16. A variable Prandtl number, along with a variable Lewis number, is used. A binary diffusion approximation is used for computing the variable Lewis number, and the binary diffusion coefficient is assumed to be that for molecular nitrogen diffusing into atomic oxygen.

The thermodynamic properties used in the BLIMP boundary-layer code are from the JANAF tables of reference 17, which are valid to 6000 K. For temperatures above 6000 K, BLIMP uses the JANAF data to extrapolate to 30 000 K. At the lower temperatures (near the wall), values of the specific heat and enthalpy are essentially the same as from references 14 and 17. At higher temperatures near the shock, however, the properties from reference 14 and those extrapolated from reference 17 are considerably different. For the calculation of Schmidt (or Lewis) number, BLIMP uses a bifurcation approximation to simplify the conservation equations and to allow the use of a reference diffusion coefficient with diffusion factors that are a function only of the species. Similar to the VSL and N-S codes, the mixture viscosity and the thermal conductivity are computed by using the formulas of references 15 and 16. However, the individual species viscosities and thermal conductivities are those from reference 18. At a temperature of 3000° R (which is comparable to the wall temperature in the present work) there is a difference of about 13.8 percent in the mixture thermal conductivity computed by the VSL and BLIMP codes at peak heating conditions; the viscosities of the mixtures are essentially the same. This difference in the thermal conductivity is partially responsible for the difference in the heating rates predicted by the VSL and BLIMP codes near peak heating conditions.

Results and Discussion

As stated previously, the goal of this work is to first demonstrate that a combination of the VSL and

N-S methods can provide accurate stagnation-point heating predictions over the very broad range of free-stream conditions of the aeropass. This is done by comparison with other detailed methods considered to be benchmark quality for the specific conditions. Then the specific adjustment factors required for the AFE trajectory to correct the stagnation-point results of the boundary-layer method are presented. Also, since the range of free-stream conditions is so broad, spanning much of the viscous continuum regime and including chemically reacting stream and wall conditions, the applicability of some of the commonly used viscous correlation parameters is examined.

Verification of VSL and N-S Results

This section presents the verification of the methods used to define the stagnation-point heating rate history for the aeroassist vehicle. The definition of these rates by a full 3-D finite reacting code applicable to continuum as well as near-continuum limits would require a large amount of computer time. Thus, two assumptions were made to permit timely calculations of the stagnation values. The first was that an effective nose radius could be determined to allow the use of axisymmetric methods. The second was that a stagnation-region N-S method with surface slip could be used to define the aerothermal conditions for the highest altitudes to be considered, even though these conditions border on or exceed the continuum limit. For the lower altitudes, a VSL method was considered to be more efficient and adequate to define the heating. In addition to demonstrating the applicability of this code combination, the section will also define the match point, that is, the trajectory condition for which it is appropriate to switch codes.

Axisymmetric approximation. The LAURA code results of reference 7 for the AFE forebody configuration at free-stream conditions typical of peak heating were used to determine an effective nose radius for the VSL code. An effective radius of 7.1 ft (2.16 m) was found, and this value was used for both the VSL method and N-S method for all cases. In figure 4, results from the VSL and N-S methods are compared. The cases presented in figure 4 are for a slightly different trajectory than the Baseline 5 trajectory used elsewhere in this paper, but the differences are minor, and the results shown in figure 4 span the range of conditions considered herein. Figure 4(a) presents the heat-transfer coefficient as a function of free-stream Reynolds number (based on a nose radius of 7.54 ft). For the highest Reynolds numbers

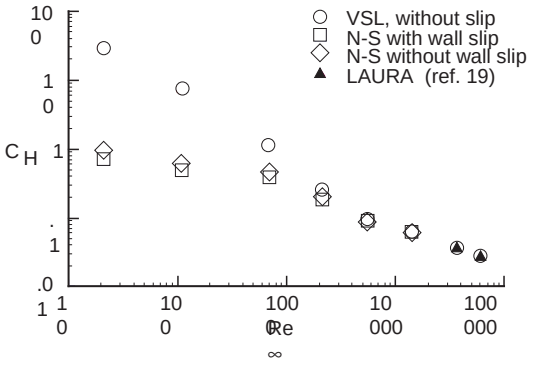

(a) Free-stream Reynolds number as independent parameter.

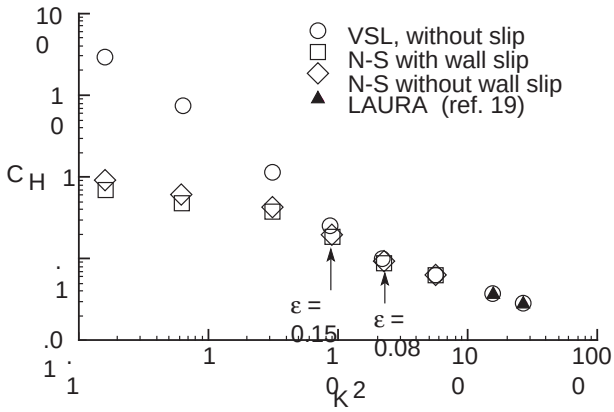

(b) Cheng's rarefaction parameter, K^2, as independent parameter.

Figure 4. Comparison of VSL and N-S methods over the range of free-stream conditions of the present study.

considered ($Re_\infty > 60\,000$), the VSL calculations are compared with newer results from the 3-D LAURA code (ref. 19). The assumed free-stream conditions of reference 19 are somewhat different, and the LAURA code had undergone further refinement in the interim, but it is clear from figure 4(a) that an effective nose radius of 7.1 ft in the VSL code again gives good agreement with the 3-D LAURA results. No LAURA code results were available for comparison at higher altitudes. It may be noted that use of this effective nose radius accounts for not only the 3-D effects, but also other differences in code characteristics.

Match point. The VSL heating rate results are in good agreement with the N-S results for Reynolds numbers greater than 5000, but for smaller Reynolds numbers, the VSL method begins to diverge, producing values of heat-transfer coefficient

greater than 1 for the lowest Reynolds number cases. The small values of Reynolds number encompassed by the present results are indicative of the large role of transport effects in the stagnation-region flow field. This is illustrated in figure 4(b) by presenting the results with Cheng's rarefaction parameter, K^2, as the independent variable. This parameter is defined in reference 20 as

$$K^2 = \zeta_\infty \frac{\rho_\infty U_\infty R_n}{\mu_*} \frac{T_*}{T_o} \tag{3}$$

where the subscript $*$ refers to the reference temperature, taken as

$$T_* = \frac{T_s + T_w}{2} \tag{4}$$

For the present work, K^2 was evaluated in the same manner as in reference 21:

$$K^2 = \frac{\mathrm{Re}_\infty}{\gamma_\infty M_\infty^2 C_*} \tag{5}$$

where C_* is the Chapman-Rubesin constant

$$C_* = \frac{\mu_* T_\infty}{\mu_\infty T_*} \tag{6}$$

For simplicity in evaluating T_*, the wall temperature was assumed constant at $T_w = 1500$ K, and the temperature behind the shock, T_s, is replaced by the ideal gas stagnation temperature, T_o. Equations (3) and (5) are equivalent for a perfect gas.

In reference 20, Cheng used the quantity ζK^2 to define the boundary of the vorticity-interaction regime as follows:

Regime I: $O(1) \le \zeta K^2 < \infty$
Regime II: $O(\zeta) \le \zeta K^2 \le O(1)$

Cheng defines regime I as the boundary-layer and vorticity-interaction domains, and regime II as the incipient-merged-layer domain. Since effective values of ζ are of the order of 0.1, the onset boundary of the incipient-merged-layer regime may be taken roughly as $K^2 = 10$. This is seen in figure 4(b) to be approximately the point at which the VSL predictions of heating rate diverge from the N-S predictions.

The VSL method used here omits both wall-slip and shock-slip effects. The effects of wall slip are shown in figure 4 by the N-S results, which are presented for cases both with and without wall-slip boundary conditions. It may be seen that wall slip makes a moderate impact on the heat-transfer rate for values of K^2 less than 10. However, the small magnitude of the wall-slip effect makes it clear that this is not the primary cause of the VSL divergence. In reference 22, it is also shown that wall-slip and shock-slip effects become significant at about the same degree of rarefaction. The rarefaction parameter used in reference 22 is ε, which is defined as

$$\varepsilon = \frac{1}{\sqrt{\mathrm{Re}_{\mathrm{ref}}}} \tag{7}$$

where

$$\mathrm{Re}_{\mathrm{ref}} = \frac{\rho_\infty U_\infty R_n}{\mu_{\mathrm{ref}}} \tag{8}$$

$$\mu_{\mathrm{ref}} = \mu\left(T_{\mathrm{ref}}\right) \tag{9}$$

$$T_{\mathrm{ref}} = \frac{U_\infty^2}{c_{p\infty}} \tag{10}$$

The Sutherland relation (ref. 14) is to be used to evaluate the viscosity μ_{ref} at the temperature T_{ref}.

Reference 22 presents perfect gas solutions of the VSL equations, and these solutions indicate that the effects of wall-slip and shock-slip influence the stagnation-point heating rate for values of $\varepsilon \ge$ about 0.15. In figure 4(b), values of ε are shown for the cases of $K^2 = 9$ and 22. It is seen that the divergence of the VSL solutions commences for values of ε greater than about 0.1.

Since no shock slip is assumed in the present VSL calculation method, the shock wave is modeled as a discontinuity, whereas in actuality for small values of K^2, the shock wave acquires significant thickness compared with the entire shock layer. This is illustrated in figure 5, which shows normal temperature profiles as computed by the VSL and N-S methods for the two cases of $\varepsilon = 0.08$ and 0.13. Since the VSL assumes an instantaneous jump for the shock, the shock-wave thickness is always zero for this method. This is appropriate for large values of the flow Reynolds number (or small values of ε) when the outer portion of the shock-layer flow may be assumed inviscid. However, the shock wave, as computed by the N-S solution, thickens rapidly with diminishing density, as is clearly evident for $\varepsilon = 0.13$. Thus, the VSL method, which omits the viscous diffusion terms in the normal momentum equation, begins to predict inaccurate wall heat transfer when its shock-jump model becomes inadequate. In comparing the present results, for nonequilibrium flow chemistry and finite wall catalysis, with the perfect

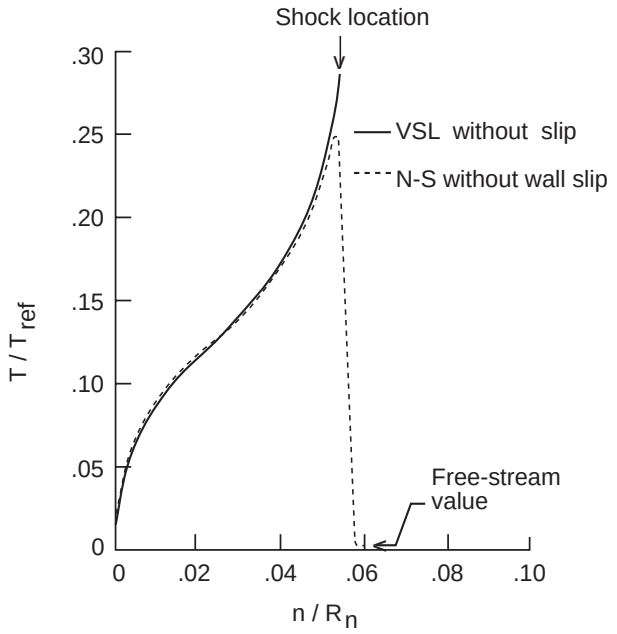

(a) ε (Davis' parameter) = 0.08.

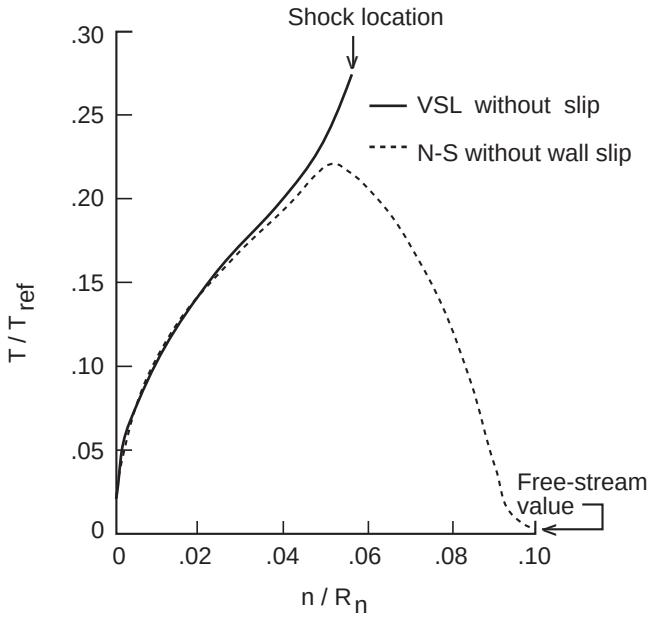

(b) ε (Davis' parameter) = 0.13.

Figure 5. Comparison of temperature profiles.

gas solutions of reference 22, it is seen that the value of ε for which shock and wall slip become important is about the same. Thus, it appears that flow chemistry is not a major driver in determining the onset of slip effects.

In the present work, the VSL method is used only when the value of ε is less than 0.07, so as to avoid errors categorized as shock-slip errors. Also, to avoid wall-slip errors in the results at high altitudes, only N-S cases with wall slip are included.

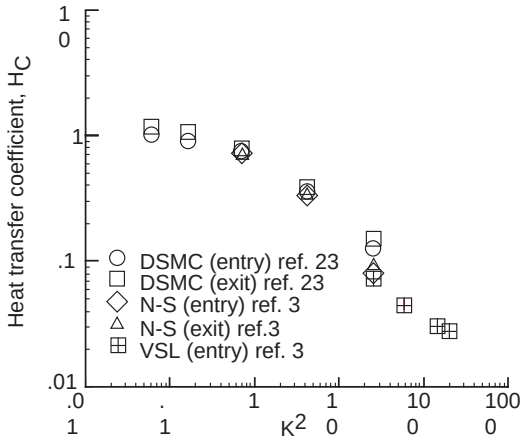

Figure 6. Comparison of direct simulation Monte Carlo prediction with continuum method results for AFE trajectory conditions. $T_w = 1000$ K for all cases.

Near-continuum range comparison. The range of the present results includes cases for which K^2 is less than 1, and thus the data extend beyond the accepted boundary of the merged layer regime. For the present conditions, at $K^2 = 1$ the free-stream mean free path is approximately 0.78 m, or about 1/3 the nose radius. Thus, it is appropriate to question the validity of the continuum-flow assumption for the most rarefied cases. In figure 6, results (which were reported in ref. 3) from the present VSL and N-S methods are compared with the predictions reported in reference 23 from the direct simulation Monte Carlo (DSMC) method. The results in this reference were obtained in support of the AFE project, and thus the configuration and trajectory conditions were similar to those for the present results. However, for all results shown in figure 6, the wall temperature was assumed to be 1000 K. Figure 6 shows that the N-S results are in good agreement with the DSMC results for values of K^2 less than 1. The greatest disagreement between the continuum and DSMC methods occurs when K^2 is about 25, which corresponds to an altitude of 295 000 ft (90 km). Since this is a region where one should expect good results for either the N-S or the DSMC approach, the discrepancy would appear to be the result of differing assumptions. One such assumption concerns thermal equilibrium in the shock layer. The present continuum methods assume thermal equilibrium, but the DSMC calculations make no such assumption.

Indeed they predict large differences in the translational, rotational, and vibrational temperatures at an altitude of 90 km (see ref. 23). It is reasonable to expect that this thermal nonequilibrium makes a significant impact on the chemical reactions, and hence on the wall heat-transfer rate. At higher altitudes the thermal nonequilibrium is greater, but the chemical reactions are retarded, with the flow nearly frozen chemically. For lower altitudes, reference 23 shows that thermal nonequilibrium is greatly diminished in the shock layer, and at an altitude of 78 km, thermal equilibrium has been essentially attained near the wall.

Results Obtained for AFE Trajectory

All the stagnation-point convective-heating results which have been computed by the three computational methods are presented in table III. For convenience, both English and metric units are presented in this table, and the data have been separated into entry and exit phases of the trajectory. All the calculated results are shown in figure 7, where the heat-transfer rate, q_c, is shown as a function of trajectory time. This figure illustrates that the calculations are sufficient in number to define the heat pulse of the aeroassist maneuver. Figure 7 also shows that the detailed flow-field methods (VSL and N-S) tend to predict a greater heating rate than the boundary-layer method. Near the peak of the heat pulse, the VSL method predicts higher heating than the BLIMP method by about 6 percent. Much of this difference can be attributed to the difference in nose radius assumed and in the transport properties used in the two methods. However, at the early entry as well as the later exit times, the discrepancies are much larger. These times represent flow-field conditions for which boundary-layer assumptions are not applicable.

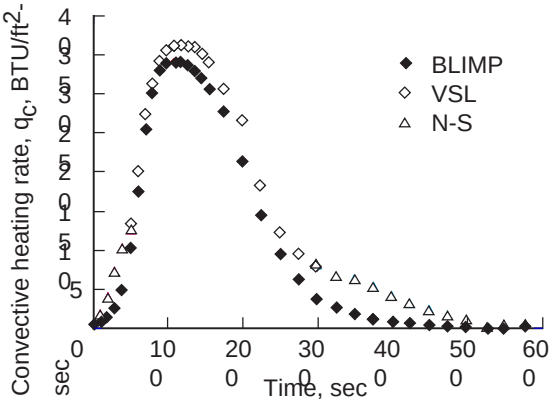

Figure 7. Heat-transfer rate as a function of trajectory time.

The differences in predicted heating rate are more clearly seen in figure 8, which shows the heat-transfer coefficient, C_H, presented as a function of free-stream Reynolds number, Re_∞. It may be seen here that the results for the entry leg (i.e., while the vehicle is descending) do not correlate well with the outbound, or exit, leg results for corresponding values of Reynolds number. The difference is greatest for the BLIMP results, but may be discerned to a much lesser extent for the VSL or N-S solutions as well. The velocity is significantly different for the two legs, except, of course, near perigee. For any given altitude above 260 000 ft, the velocity exceeds 32 000 ft/sec on the entry leg and is less than 26 000 ft/sec for the exit leg. This velocity difference implies large differences in shock-layer temperatures and species concentrations, so it is to be expected that free-stream Reynolds number may not be an adequate correlation parameter for the entry leg and exit leg results. However, it is not obvious why the lower velocity, exit results for the boundary-layer method would be so much lower than the entry leg results, while the VSL and N-S results are in much better agreement for the two legs. This discrepancy may arise from the several shortcomings of the boundary-layer method when it is employed at these extremely high-altitude flight conditions. Major contributors are the assumption of equilibrium edge conditions, no slip effects, and the neglect of displacement thickness effects for the boundary-layer method.

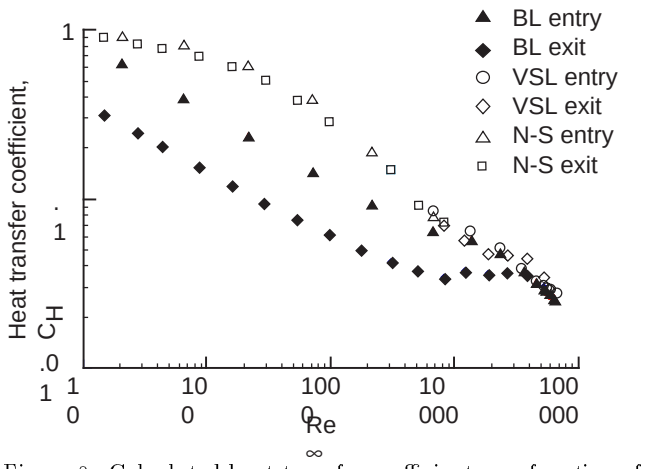

Figure 8. Calculated heat-transfer coefficient as a function of free-stream Reynolds number.

Figure 9 shows the results with K^2 as the independent variable. For the N-S solutions for $K^2 < 10$, this parameter improves the agreement between the results from the entry and exit legs. Use of this parameter does not help the correlation for the boundary-layer method results. Figure 10 shows the heat-transfer coefficient with a postshock Reynolds

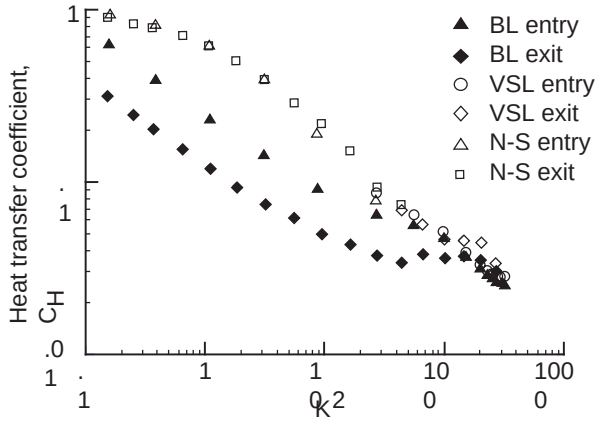

Figure 9. Present data with rarefaction parameter K^2.

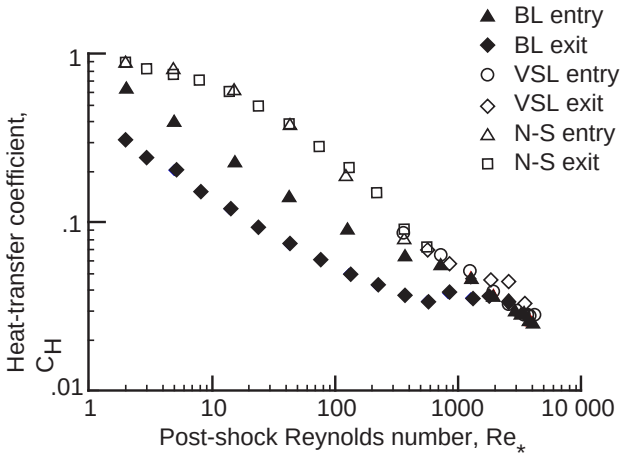

Figure 10. Correlation of data with postshock Reynolds number as the independent parameter.

number, Re_*, as the independent parameter. The correlation using this parameter is seen to be similar to that obtained using K^2 (fig. 9.)

As explained previously, it was considered desirable to use the boundary-layer method for the AFE heat shield design calculations because it provided a quick, computationally inexpensive means to compute heating rate over the entire forward face of the vehicle, including an approximation to the nonaxisymmetric nature of the AFE configuration. As shown in figures 8–10, the boundary-layer calculation is appropriate for conditions near the AFE perigee, but it incurs large errors at higher altitudes, where it is important to consider low-density phenomena, including wall slip, shock slip, and incipient merged-layer flow. Thus, in order to use the boundary-layer method to estimate convective heat-transfer rate over the entire aeropass trajectory, it is necessary that an adjustment factor correct the stagnation-point heating for these effects. The value of the adjustment factor was obtained by comparison of the boundary-layer predictions with those from the VSL and N-S codes. Specifically, the adjustment factor is the ratio of the VSL result to the BLIMP result for $\varepsilon < 0.07$ and is the ratio of the N-S result to the BLIMP result for $\varepsilon > 0.07$. It may be noted that using the adjustment factor to scale the stagnation-point heating, and then using the boundary-layer method to compute the heating distribution, implies that the adjustment factor adequately corrects the heating rate over the entire forward surface. In fact, it is not known if this is true, for only very limited 3-D benchmark results are available to compare with the boundary-layer calculations for locations away from the stagnation point, and the solutions available do not span the necessary range of free-stream conditions.

The adjustment factor is presented as a function of rarefaction parameter K^2 in figures 11 and 12. In figure 11 the adjustment factor is based on convective heat-transfer rate, whereas in figure 12 the total heat-transfer rate is used to form this factor. As could be expected, there are only minor differences between the results for the two forms of the adjustment factor. In either figure, this factor is near 1.0 for the highest density conditions. With decreasing value of K^2, the value of the adjustment factor rises, reaching a peak near $K^2 = 2$, and then decreases. Although the increase occurs for both the entry phase and the exit phase, the peak value is much greater for the exit phase.

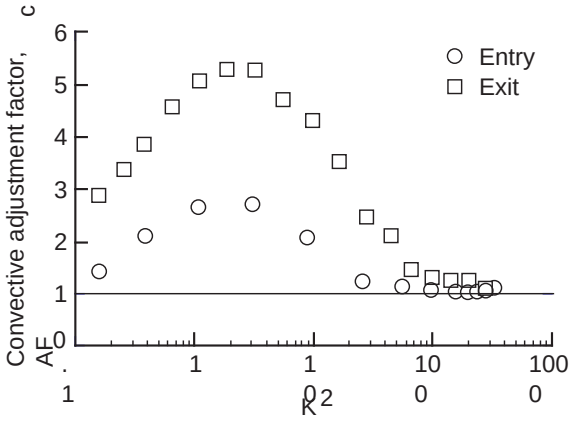

Figure 11. Convective adjustment factor as a function of the rarefaction parameter K^2 for both entry and exit phases of the aeropass.

In the past, various investigators (e.g., refs. 24 and 25) have also found a similar result; the ratio of q_c predicted by viscous flow-field methods to

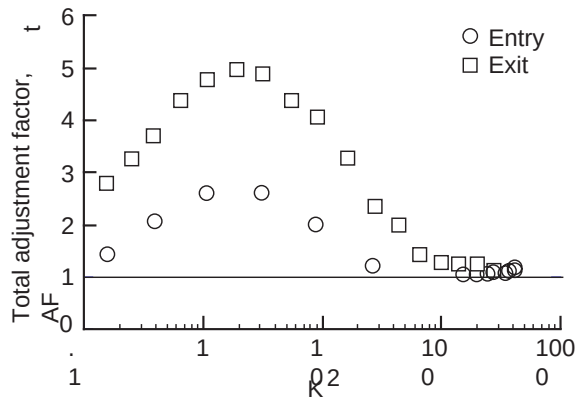

Figure 12. Total adjustment factor as a function of the rarefaction parameter K^2 for both entry and exit phases of the aeropass.

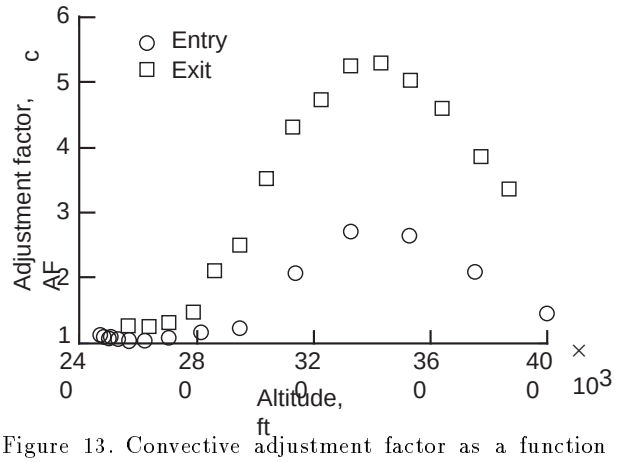

Figure 13. Convective adjustment factor as a function of altitude for entry and exit phases of the aeropass.

that predicted by the boundary-layer method tends to values greater than 1.0 for rarefied conditions, but falls, even to values less than 1.0, as noncontinuum flow is approached. In reference 24, this trend is shown to be confirmed by the experimental data available. The present adjustment factors follow similar trends qualitatively. While this paper evaluates the error in heat-transfer rate prediction that occurs if the boundary-layer method is employed at very high-altitude flight conditions, it does not attempt an analysis of the specific failures of the boundary-layer assumptions.

It may be noted that when the adjustment factor is not near 1.0, there is a disparity in the computed wall temperature between the BLIMP result and the VSL or N-S result. Thus, when the adjustment factor and the BLIMP code are employed, this correction accounts not only for the errors in the boundary-layer assumption, but also for the difference in computed wall temperature.

Finally, figure 13 presents the adjustment factor as a function of altitude. Design calculations for AFE component heating at various altitudes have employed the adjustment factor as shown in this figure.

Concluding Remarks

This work presents the results of stagnation-point heat-transfer calculations for the Aeroassist Flight Experiment (AFE) vehicle over its entire aeropass trajectory. These results have been obtained to predict heating rates for heat shield and experiment design of the AFE during its aeropass maneuver. The predictions cover the altitude range 246 000 to 400 000 ft (75.2 to 121.9 km) and the velocity range 24 500 to 32 500 ft/sec (7484 to 9917 m/sec). For these conditions, a viscous-shock-layer (VSL) code was run for the more dense (lower altitude) cases, and a stagnation-region code employing the full Navier-Stokes (N-S) equations was run for the more rarefied (higher altitude) cases. The calculated results from these methods were used to form an adjustment factor, which corrected the stagnation-point results obtained with the BLIMP boundary-layer code to an accurate estimate, even though the range included free-stream conditions far too rarefied to justify the boundary-layer assumptions. The BLIMP code was used because it provided an engineering approach that could include a reacting boundary layer and wall catalysis. The code was quick, computationally inexpensive, and a convenient way to compute heating distributions over the entire forward face of the AFE configuration. All the methods employed similar models for wall catalysis and wall temperature and included an estimate of the radiative contribution to the total heating. Some differences in geometry were used in the boundary-layer method, but their effects on heating were not large.

The combination of the VSL and N-S methods was found to be an accurate computational tool to cover the wide range of free-stream conditions spanned by the present results. The VSL method, used for the more dense cases, employed an axisymmetric model with an effective nose radius of 7.1 ft, which was found to give good agreement with the benchmark LAURA code results for the full 3-D AFE configuration. The VSL method was used for those times on the trajectory for which the rarefaction parameter ε was less than 0.07. For cases where ε was larger than 0.07, the N-S method was used. It was shown that wall slip made a moderate impact on heating rate, so only N-S cases with wall-slip boundary condition were included.

The Navier-Stokes method predicted the stagnation-point heating in good agreement with the direct simulation Monte Carlo method for the highest altitude cases (400 000 ft). It is concluded, therefore, that the continuum method heating predictions are accurate for the most rarefied of the present cases.

The adjustment factor was obtained as the ratio of the VSL or N-S prediction to the corresponding BLIMP prediction. This adjustment factor, combined with BLIMP heating-value predictions over the forebody, was suggested as an engineering approach to provide design heat-transfer values for the vehicle forebody. The present results showed that convective heating results obtained from the VSL and BLIMP methods were in good agreement for the highest density cases, where the Reynolds number approached a value of 10^5. For these cases the adjustment factor was about 1.06, and most of this difference may be attributed to differences in geometry and transport property assumptions. However, with decreasing density, the adjustment factor rose rapidly, reaching a peak for a value of Cheng's parameter, K^2, of about 2. With increasingly more rarefied conditions, the adjustment factor again approached unity.

NASA Langley Research Center
Hampton, VA 23681-0001
July 16, 1992

References

1. Walberg, Gerald D.: A Survey of Aeroassisted Orbit Transfer. *J. Spacecr. & Rockets,* vol. 22, no. 1, Jan.-Feb. 1985, pp. 3–18.

2. Jones, Jim J.: The Rationale for an Aeroassist Flight Experiment. AIAA-87-1508, June 1987.

3. Gupta, Roop N.; and Simmonds, Ann L.: Stagnation Flowfield Analysis for an Aeroassist Flight Experiment Vehicle. AIAA-88-2613, June 1988.

4. Gupta, Roop N.: Navier-Stokes and Viscous Shock-Layer Solutions for Radiating Hypersonic Flows. AIAA-87-1576, June 1987.

5. Murray, Alvin L.: *Further Enhancements of the BLIMP Computer Code and User's Guide.* AFWAL-TR-88-3010, U.S. Air Force, June 1988. (Available from DTIC as AD B126 768.)

6. Cheatwood, F. McNeil; DeJarnette, Fred R.; and Hamilton, H. Harris, II: *Geometrical Description for a Proposed Aeroassist Flight Experiment Vehicle.* NASA TM-87714, 1986.

7. Gnoffo, Peter A.: A Code Calibration Program in Support of the Aeroassist Flight Experiment. AIAA-89-1673, June 1989.

8. Justus, C. G.; Fletcher, G. R.; Gramling, F. E.; and Pace, W. B.: *The NASA/MSFC Global Reference Atmospheric Model—MOD 3 (With Spherical Harmonic Wind Model).* NASA CR-3256, 1980.

9. Gupta, Roop N.; Scott, Carl D.; and Moss, James N.: *Slip-Boundary Equations for Multicomponent Nonequilibrium Airflow.* NASA TP-2452, 1985.

10. Kolodziej, Paul; and Stewart, David A.: Nitrogen Recombination on High-Temperature Reusable Surface Insulation and the Analysis of Its Effect on Surface Catalysis. AIAA-87-1637, June 1987.

11. Hamilton, H. H., II; Gupta, Roop N.; and Jones, Jim J.: Flight Stagnation-Point Heating Calculations on Aeroassist Flight Experiment Vehicle. *J. Spacecr. & Rockets,* vol. 28, no. 1, Jan.-Feb. 1991, pp. 125–128.

12. Lee, K. P.; Gupta, R. N.; Zoby, E. V.; and Moss, J. N.: Hypersonic Viscous Shock-Layer Solutions Over Long Slender Bodies—Part II: Low Reynolds Number Flows. *J. Spacecr. & Rockets,* vol. 27, no. 2, Mar.-Apr. 1990, pp. 185–193.

13. Hamilton, H. Harris, II; and Spall, John R.: *Time-Dependent Solution for Axisymmetric Flow Over a Blunt Body With Ideal Gas, CF_4, or Equilibrium Air Chemistry.* NASA TM-87675, 1986.

14. Gupta, Roop N.; Yos, Jerrold M.; Thompson, Richard A.; and Lee, Kam-Pui: *A Review of Reaction Rates and Thermodynamic and Transport Properties for an 11-Species Air Model for Chemical and Thermal Nonequilibrium Calculations to 30 000 K.* NASA RP-1232, 1990.

15. Armaly, Bassem F.; and Sutton, Kenneth: Viscosity of Multicomponent Partially Ionized Gas Mixtures. AIAA-80-1495, July 1980.

16. Mason, E. A.; and Saxena, S. C.: Approximate Formula for the Thermal Conductivity of Gas Mixtures. *Phys. Fluids,* vol. 1, no. 5., Sept.-Oct. 1958, pp. 361–369.

17. Chase, M. W., Jr.; Davies, C. A.; Downey, J. R., Jr.; Frurip, D. J.; McDonald, R. A.; and Syverud, A. N.: *JANAF Thermochemical Tables, Third Edition, Part II, Cr–Zr.* J. Phys. & Chem. Ref. Data, vol. 14, suppl. no. 1, 1985.

18. Bartlett, Eugene P; and Kendall, Robert M.: *An Analysis of the Coupled Chemically Reacting Boundary Layer and Charring Ablator. Part III—Nonsimilar Solution of the Multicomponent Laminar Boundary Layer by an Integral Matrix Method.* NASA CR-1062, 1968.

19. Hamilton, H. Harris, II; and Greendyke, Robert B: *Calculation of Convective and Radiative Heating on the Forebody Heatshield of the Aeroassisted Flight Experiment Vehicle.* NASA TM-104103, 1991.

20. Cheng, Hsien K.: *Hypersonic Shock-Layer Theory of the Stagnation Region at Low Reynolds Number.* Rep. No. AF-1285-A-7 (Contract Nonr-2653(00)), Cornell Aeronautical Lab., Inc., Apr. 1961. (Available from DTIC as AD 256 745.)

21. Vidal, R. J.; and Wittliff, C. E.: Hypersonic Low Density Studies of Blunt and Slender Bodies. *Rarefied Gas Dynamics, Volume II,* J. A. Laurmann, ed., Academic Press, 1963, pp. 343–378.

22. Davis, R. T.: Numerical Solution of the Hypersonic Viscous Shock-Layer Equations. *AIAA J.,* vol. 8, no. 5, May 1970, pp. 843–851.

23. Dogra, Virendra K.; Moss, James N.; and Simmonds, Ann L.: Direct Simulation of Aerothermal Loads for an Aeroassist Flight Experiment Vehicle. AIAA-87-1546, June 1987.

24. Cheng, H. K.; and Chang, A. L.: Stagnation Region in Rarefied, High Mach Number Flow. *AIAA J.,* vol. 1, no. 1, Jan. 1963, pp. 231–233.

25. Gilbert, Leon M.; and Goldberg, Leon: A Reynolds Number Scaling Theory for Hypersonic Ablation. AIAA-67-155, Jan. 1967.

Table I. Free-Stream Conditions

(a) Entry phase

Time, sec	English units				Metric units			
	Altitude, ft	Velocity, ft/sec	Density, slugs/ft^3	Pressure, lb/ft^2	Altitude, m	Velocity, m/sec	Density, kg/m^3	Pressure, N/m^2
0	399 934	32 461	3.828×10^{-11}	5.148×10^{-5}	121 900	9894	1.973×10^{-8}	2.465×10^{-3}
9.6	375 386	32 496	9.756×10^{-11}	9.900×10^{-5}	114 418	9905	5.028×10^{-8}	4.740×10^{-3}
19.2	352 851	32 516	2.848×10^{-10}	2.249×10^{-4}	107 549	9911	1.468×10^{-7}	1.077×10^{-2}
28.8	332 406	32 531	8.497×10^{-10}	5.161×10^{-4}	101 317	9915	4.379×10^{-7}	2.471×10^{-2}
38.4	314 077	32 537	2.416×10^{-9}	1.423×10^{-3}	95 731	9917	1.245×10^{-6}	6.815×10^{-2}
49.9	294 944	32 511	7.112×10^{-9}	4.061×10^{-3}	89 899	9909	3.665×10^{-6}	1.944×10^{-1}
59.5	281 496	32 440	1.414×10^{-8}	8.353×10^{-3}	85 800	9888	7.285×10^{-6}	3.999×10^{-1}
69.1	270 478	32 295	2.479×10^{-8}	1.488×10^{-2}	82 442	9844	1.278×10^{-5}	7.125×10^{-1}
78.7	262 092	32 052	3.804×10^{-8}	2.302×10^{-2}	79 886	9769	1.961×10^{-5}	1.102×10^{0}
88.3	256 541	31 708	5.039×10^{-8}	3.067×10^{-2}	78 194	9665	2.597×10^{-5}	1.468×10^{0}
97.9	253 461	31 289	5.889×10^{-8}	3.597×10^{-2}	77 255	9537	3.035×10^{-5}	1.722×10^{0}
107.5	251 288	30 825	6.574×10^{-8}	4.024×10^{-2}	76 593	9395	3.388×10^{-5}	1.927×10^{0}
117.1	249 634	30 329	7.148×10^{-8}	4.384×10^{-2}	76 088	9244	3.684×10^{-5}	2.099×10^{0}
126.7	248 425	29 813	7.599×10^{-8}	4.667×10^{-2}	75 720	9087	3.916×10^{-5}	2.235×10^{0}
136.3	247 596	29 289	7.924×10^{-8}	4.873×10^{-2}	75 467	8927	4.084×10^{-5}	2.333×10^{0}
145.9	246 946	28 763	8.188×10^{-8}	5.039×10^{-2}	75 269	8767	4.220×10^{-5}	2.413×10^{0}
155.5	246 780	28 245	8.253×10^{-8}	5.082×10^{-2}	75 219	8609	4.253×10^{-5}	2.433×10^{0}

(b) Exit phase

Time, sec	English units				Metric units			
	Altitude, ft	Velocity, ft/sec	Density, slugs/ft^3	Pressure, lb/ft^2	Altitude, m	Velocity, m/sec	Density, kg/m^3	Pressure, N/m^2
174.7	250 283	27 317	6.917×10^{-8}	4.239×10^{-2}	76 286	8326	3.565×10^{-5}	2.030×10^{0}
199.7	256 520	26 447	5.044×10^{-8}	3.070×10^{-2}	78 187	8061	2.600×10^{-5}	1.470×10^{0}
224.6	263 276	25 850	3.581×10^{-8}	2.164×10^{-2}	80 247	7879	1.846×10^{-5}	1.036×10^{0}
249.6	270 393	25 443	2.490×10^{-8}	1.494×10^{-2}	82 416	7755	1.283×10^{-5}	7.153×10^{-1}
274.6	278 635	25 150	1.636×10^{-8}	1.004×10^{-2}	84 928	7666	8.431×10^{-6}	4.807×10^{-1}
299.5	286 086	24 981	1.118×10^{-8}	6.534×10^{-3}	87 199	7614	5.764×10^{-6}	3.128×10^{-1}
324.5	294 707	24 858	7.199×10^{-9}	4.114×10^{-3}	89 827	7577	3.710×10^{-6}	1.970×10^{-1}
349.4	303 772	24 776	4.344×10^{-9}	2.501×10^{-3}	92 590	7552	2.239×10^{-6}	1.197×10^{-1}
374.4	313 017	24 722	2.568×10^{-9}	1.504×10^{-3}	95 408	7535	1.324×10^{-6}	7.201×10^{-2}
399.4	322 577	24 686	1.480×10^{-9}	9.158×10^{-4}	98 321	7524	7.628×10^{-7}	4.385×10^{-2}
424.3	332 453	24 660	8.475×10^{-10}	5.600×10^{-4}	101 332	7516	4.368×10^{-7}	2.681×10^{-2}
449.3	342 672	24 639	4.832×10^{-10}	3.450×10^{-4}	104 446	7510	2.490×10^{-7}	1.652×10^{-2}
474.2	353 243	24 621	2.792×10^{-10}	2.213×10^{-4}	107 668	7504	1.439×10^{-7}	1.060×10^{-2}
499.2	364 168	24 604	1.626×10^{-10}	1.447×10^{-4}	110 998	7499	8.379×10^{-8}	6.928×10^{-3}
528.0	377 206	24 586	8.999×10^{-11}	9.323×10^{-5}	114 972	7494	4.638×10^{-8}	4.464×10^{-3}
549.1	387 054	24 573	6.036×10^{-11}	7.049×10^{-5}	117 974	7490	3.111×10^{-8}	3.375×10^{-3}
577.9	400 863	24 554	3.678×10^{-11}	5.049×10^{-5}	122 183	7484	1.895×10^{-8}	2.417×10^{-3}

Table II. Correlation Parameters Used for Present Calculations

Time, sec	Altitude, ft	Mach no.	Re_∞	K^2	Re_*	ε
Entry phase						
0	399 934	24.15	21	0.16	2	1.007
9.6	375 386	27.89	64	.39	5	.631
19.2	352 851	31.51	216	1.09	15	.369
28.8	332 406	34.30	715	3.14	43	.214
38.4	314 077	36.03	2 186	8.83	123	.127
49.9	294 944	36.39	6 757	26.81	362	.074
59.5	281 496	35.67	13 602	55.80	719	.052
69.1	270 478	35.21	23 667	99.01	1260	.040
78.7	262 092	34.78	35 550	151.11	1933	.032
88.3	256 541	34.31	45 895	198.25	2560	.028
97.9	253 461	33.80	52 377	230.09	2990	.026
107.5	251 288	33.26	57 126	255.39	3337	.024
117.1	249 634	32.70	60 701	276.43	3626	.023
126.7	248 425	32.12	63 100	292.89	3854	.023
136.3	247 596	31.54	64 403	304.82	4017	.022
145.9	246 946	30.97	65 154	314.40	4147	.022
155.5	246 780	30.40	64 439	317.16	4179	.022
Exit phase						
174.7	250 283	29.46	53 052	269.56	3498	0.024
199.7	256 520	28.62	38 317	200.32	2548	.028
224.6	263 276	28.07	27 059	144.10	1807	.033
249.6	270 393	27.74	18 726	100.71	1256	.039
274.6	278 635	27.58	12 210	65.85	824	.049
299.5	286 086	27.64	8 264	44.18	564	.059
324.5	294 707	27.81	5 232	27.57	363	.073
349.4	303 772	27.67	3 085	16.37	219	.094
374.4	313 017	27.45	1 772	9.52	129	.123
399.4	322 577	26.79	985	5.51	75	.162
424.3	332 453	26.00	541	3.18	43	.214
449.3	342 672	25.06	293	1.83	24	.283
474.2	353 243	23.81	160	1.09	14	.373
499.2	364 168	22.51	87	0.65	8	.488
528.0	377 206	20.89	44	0.37	5	.656
549.1	387 054	19.69	28	0.25	3	.801
577.9	400 863	18.18	15	0.15	2	1.027

Table III. Calculated Stagnation-Point Heating Rate

(a) Entry phase; English units

Time, t, sec	BLIMP			Viscous shock layer			Navier-Stokes			Adjustment factors	
	q_c, BTU/ft^2-sec	q_t, BTU/ft^2-sec	T_w, °F	q_c, BTU/ft^2-sec	q_t, BTU/ft^2-sec	T_w, °F	q_c, BTU/ft^2-sec	q_t, BTU/ft^2-sec	T_w, °F	AF_c	AF_t
0	0.54	0.54	155				0.77	0.78	714	1.426	1.444
9.6	.86	.87	753				1.79	1.81	991	2.081	2.080
19.2	1.48	1.53	932				3.92	3.97	1308	2.649	2.595
28.8	2.73	2.86	1171				7.36	7.52	1617	2.696	2.629
38.4	4.96	5.33	1475				10.28	10.73	1766	2.073	2.013
49.9	10.28	11.33	1841	13.50	14.75	1988	12.60	13.84	1959	1.226	1.222
59.5	17.73	19.73	2179	20.05	22.43	2258				1.131	1.137
69.1	25.61	28.95	2446	27.40	31.37	2496				1.070	1.084
78.7	30.04	34.83	2585	31.26	36.96	2620				1.041	1.061
88.3	32.91	38.75	2667	34.08	41.02	2701				1.036	1.059
97.9	33.91	40.13	2695	35.40	42.77	2735				1.044	1.066
107.5	34.12	40.38	2700	36.05	43.46	2748				1.056	1.076
117.1	34.06	40.16	2696	36.23	43.44	2748				1.064	1.082
126.7	33.66	39.46	2682	36.05	42.89	2737				1.071	1.087
136.3	32.91	38.31	2659	35.89	41.92	2719				1.091	1.094
145.9	31.94	36.91	2631	34.96	40.8	2697				1.095	1.105
155.5	30.75	35.24	2592	34.06	39.33	2668				1.108	1.116

(b) Exit phase; English units

Time, t, sec	BLIMP			Viscous shock layer			Navier-Stokes			Adjustment factors	
	q_c, BTU/ft^2-sec	q_t, BTU/ft^2-sec	T_w, °F	q_c, BTU/ft^2-sec	q_t, BTU/ft^2-sec	T_w, °F	q_c, BTU/ft^2-sec	q_t, BTU/ft^2-sec	T_w, °F	AF_c	AF_t
174.7	27.69	30.87	2495	30.52	34.23	2562				1.102	1.109
199.7	21.16	23.20	2284	26.45	28.82	2434				1.250	1.242
224.6	14.46	15.82	2024	18.28	19.86	2177				1.264	1.255
249.6	9.52	10.45	1794	12.36	13.45	1932				1.298	1.287
274.6	6.34	6.97	1555	9.41	10.14	1770				1.484	1.455
299.5	3.82	4.27	1343	7.82	8.34	1662	8.13	8.65	1687	2.128	2.027
324.5	2.64	2.95	1185				6.60	6.96	1574	2.500	2.358
349.4	1.80	2.00	1033				6.37	6.60	1552	3.539	3.300
374.4	1.25	1.38	901				5.40	5.55	1466	4.320	4.021
399.4	.88	.96	782				4.14	4.24	1336	4.705	4.417
424.3	.61	.66	671				3.19	3.25	1225	5.230	4.926
449.3	.44	.47	578				2.33	2.37	1095	5.237	5.043
474.2	.32	.35	501				1.64	1.66	964	5.125	4.743
499.2	.24	.26	432				1.11	1.12	832	4.625	4.308
528.0	.18	.18	363				.68	.69	683	3.778	3.833
549.1	.14	.15	319				.48	.48	588	3.429	3.200
577.9	.11	.11	269				.31	.32	483	2.818	2.909

Table III. Concluded

(c) Entry phase; metric units

Time, t, sec	BLIMP			Viscous shock layer			Navier-Stokes		
	q_c, $\frac{W}{cm^2}$	q_t, $\frac{W}{cm^2}$	T_w, K	q_c, $\frac{W}{cm^2}$	q_t, $\frac{W}{cm^2}$	T_w, K	q_c, $\frac{W}{cm^2}$	q_t, $\frac{W}{cm^2}$	T_w, K
0	0.61	0.61	342				0.87	0.88	652
9.6	.97	.99	674				2.03	2.05	806
19.2	1.68	1.73	773				4.44	4.61	982
28.8	3.09	3.25	906				8.14	8.33	1154
38.4	5.63	6.05	1085				11.66	12.17	1260
49.9	11.66	12.85	1278	15.31	16.73	1360	14.28	15.70	1344
59.5	20.11	22.37	1466	22.74	25.44	1510			
69.1	29.04	32.83	1614	31.07	35.57	1642			
78.7	34.07	39.50	1692	35.45	41.91	1711			
88.3	37.32	43.95	1737	38.65	46.52	1756			
97.9	38.45	45.50	1753	40.14	48.50	1775			
107.5	38.69	45.79	1756	40.88	49.28	1782			
117.1	38.62	45.55	1753	41.08	49.26	1782			
126.7	38.17	44.74	1746	40.88	48.64	1776			
136.3	37.32	43.44	1733	40.70	47.54	1766			
145.9	36.22	41.86	1717	39.64	46.27	1754			
155.5	34.87	39.96	1696	38.62	44.60	1738			

(d) Exit phase; metric units

Time, t, sec	BLIMP			Viscous shock layer			Navier-Stokes		
	q_c, $\frac{W}{cm^2}$	q_t, $\frac{W}{cm^2}$	T_w, K	q_c, $\frac{W}{cm^2}$	q_t, $\frac{W}{cm^2}$	T_w, K	q_c, $\frac{W}{cm^2}$	q_t, $\frac{W}{cm^2}$	T_w, K
174.7	31.40	35.00	1642	34.61	38.82	1679			
199.7	24.00	26.31	1524	29.99	32.68	1608			
224.6	16.40	17.94	1380	20.73	22.52	1465			
249.6	10.80	11.86	1252	14.02	15.25	1329			
274.6	7.19	7.90	1119	10.67	11.50	1239			
299.5	4.33	4.84	1002	8.87	9.46	1179	9.23	9.82	1193
324.5	3.00	3.35	914				7.48	7.89	1130
349.4	2.04	2.27	829				7.22	7.49	1118
374.4	1.42	1.57	756				6.12	6.30	1070
399.4	.99	1.09	690				4.69	4.81	998
424.3	.69	.75	628				3.62	3.69	936
449.3	.50	.54	577				2.64	2.68	864
474.2	.37	.39	534				1.86	1.88	791
499.2	.27	.29	496				1.26	1.28	718
528.0	.20	.21	457				.77	.78	635
549.1	.16	.17	433				.54	.55	582
577.9	.12	.13	405				.36	.36	524